Supporting Information

Realization of higher thermoelectric performance by dynamic doping of copper in n-type PbTe

Li You, Jiye Zhang, Shanshan Pan, Ying Jiang, Ke Wang, Jiong Yang, Yanzhong Pei, Qing Zhu, Matthias T. Agne, G. Jeffrey Snyder, Zhifeng Ren, Wenqing Zhang*, and Jun Luo**

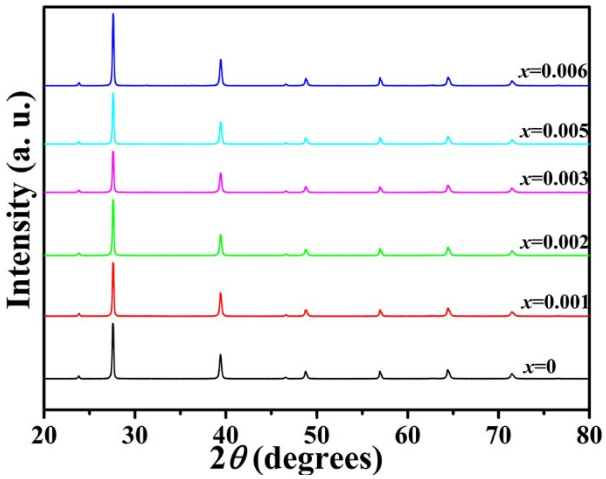

Figure S1. Room-temperature XRD patterns of $PbCu_xTe$ samples with x=0, 0.001, 0.002, 0.003, 0.005, and 0.006.

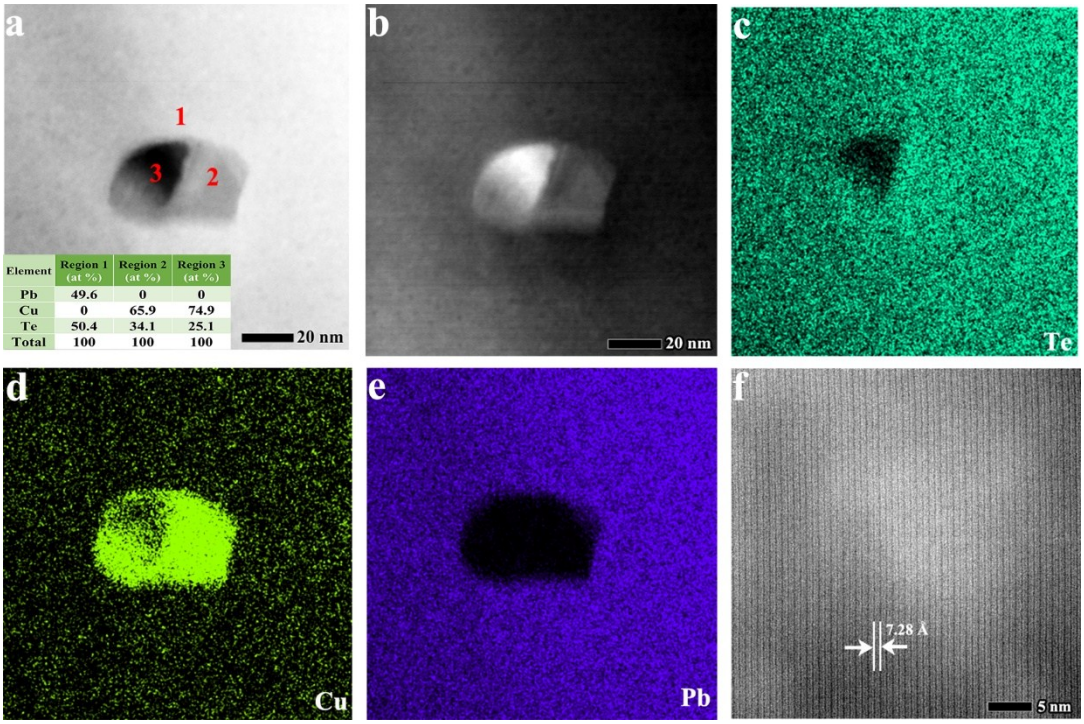

Figure S2. Morphology of Cu-related secondary phase. (a) STEM-HAADF and (b) BF images of the 10 at% Cu-doped PbTe sample. (c-e) Corresponding EDS elemental mappings of (a). (f) HRTEM image of the region 2 as shown in (a). Regions 1, 2, and 3 in (a) denote the PbTe matrix, Cu_2Te, and Cu, respectively. The inset in (a) provides the atomic ratios of regions 1, 2 and 3.

Supplementary Note 1: XRD patterns displayed in **Figure S1** show that our $PbCu_xTe$ samples crystallize in the NaCl-type structure without detectable impurities. According to our previous report, the dynamic doping effect originates from the Cu-related impurities. However, no Cu-related impurities are observed by TEM in our $PbCu_xTe$ samples with x= 0-0.006, which might be attributed to the two following reasons. On one hand, there are only trace Cu-related impurities because only a very tiny amount of Cu is added to the sample. On the other hand, the distribution of the Cu-related impurities could be extremely uniform and dispersive in the PbTe matrix because our samples have been prepared by the melt-quench method. Thus, a control sample with 10 at% Cu has been synthesized by the same method and under the same conditions as other samples in this work in order to verify the existence and phase composition of the Cu-related impurities.

Figure S2a and b shows the typical STEM-HAADF and BF images of the secondary phase embedded in the PbTe matrix, respectively. The PbTe matrix (region 1, white), Cu_2Te (region 2, grey), and Cu (region 3, black) are easily distinguished from one another based on the contrast of the HAADF image, which is further confirmed by the EDS elemental mappings. As shown in **Figure S2**c-e, in region 2, the distribution of Te shows no change compared with that of PbTe and the ratio of Cu to Te is approximately 66 : 34 (see **Table** inset the **Figure S2**a), indicating a Cu_2Te component. This is also confirmed by the atomic spacing of 7.28 Å in Fig. S2f, which corresponds to the (001) plane of Cu_2Te. In region 3, the ratio of Cu to Te increases to approximately 75 : 25, indicating the coexistence of elemental Cu and the Cu_2Te compound, as reported by Snyder et al.[1].

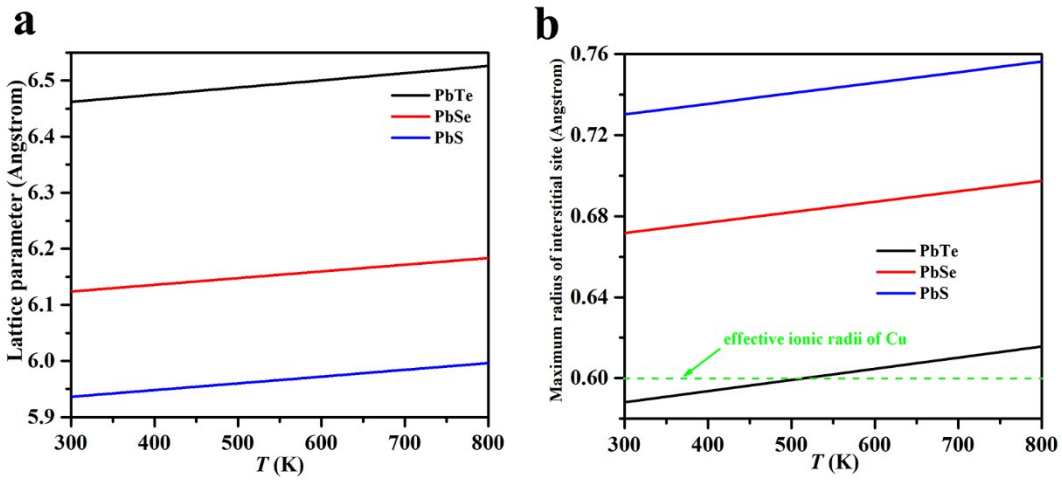

Figure S3. Calculated tetrahedral interstitial space in lead chalcogenides. Temperature dependence of (a) lattice parameters and (b) tetrahedral interstitial spaces of lead chalcogenides calculated by the rigid sphere model. The green dashed line in (b) is the effective ionic radius of Cu^+ [2] and all of the crystallographic data of lead chalcogenides are taken from the literature[3].

Supplementary Note 2: The calculated lattice parameters and the tetrahedral interstitial spaces of the lead chalcogenides are presented in **Figure S3**. Our calculation is based on the

rigid sphere model, and the half distance between the centers of the most closely packed atoms is taken as the radius of the sphere. Despite the on-site vibration of the atom and the change in the effective ionic radius with the temperature not being taken into account by this simple model, our calculation result shows clear differences between the tetrahedral interstitial spaces of the lead chalcogenides. As shown in **Figure S3**a, the lattice parameters of the lead chalcogenides increase with rising temperature due to the lattice expansion. The expansion of the crystal lattice results in enlarged interstitial space, as shown in **Figure S3**b. Therefore, the solid solubility of the interstitial Cu in lead chalcogenides increases with temperature. It is clear that the solid solubility of Cu in PbTe is the lowest among that in the lead chalcogenides because the tetrahedral interstitial space of PbTe is the smallest among that of the lead chalcogenides.

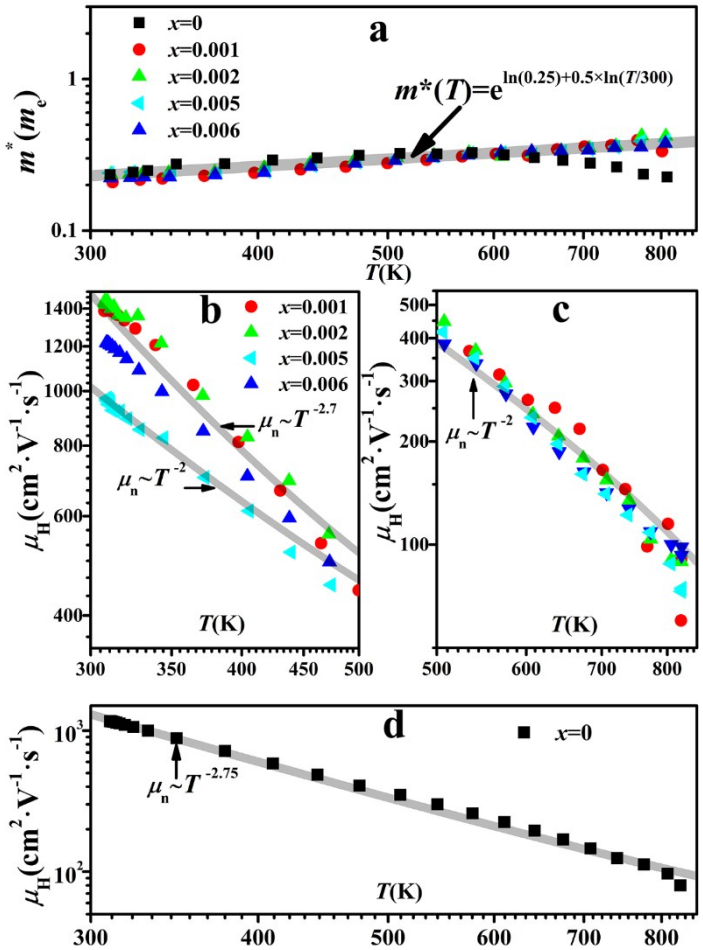

Figure S4. Temperature dependence of carrier mobility and effective mass. Temperature-dependent (a) effective-mass (from the SPB model) and (b-d) Hall-mobility values of $PbCu_xTe$ samples (x=0, 0.001, 0.002, 0.005, and 0.006). The Hall-mobility values of the doped samples are divided into two temperature regions to show clearly the different temperature-dependent relationships.

Supplementary Note 3: The temperature-dependent carrier-mobility values of the samples are shown in **Figure S4** b-d. In general, the carrier-mobility values of all of the samples decrease sharply with increasing temperature. It should be noted that the correlation between carrier mobility and temperature is distinct, but this can be interpreted by acoustic-phonon scattering at different carrier-concentration levels.

For electrons scattered by acoustic phonons, the temperature (T)-dependent mobility (μ_H) can be approximately expressed as $\mu_H \sim m^{*\upsilon} T^{\xi}$ [4]. In the non-degenerate or low-degenerate cases, the powers υ and ξ are close to -2.5 and -1.5, respectively. In the case of strong

degeneracy ($n_H > 10^{19}$ cm^{-3}), the temperature dependence of the mobility becomes weaker, and the powers υ and ξ change to -2.0 and -1.0, respectively. In addition, the electron effective mass is also temperature-dependent and follows the relationship of $m^* \sim T^{0.5}$ [calculated from the single parabolic band (SPB) model; see **Figure S4**a]. Consequently, μ_H can be scaled as $\mu_n \sim T^{-\Delta=-(0.5\upsilon+\xi)}$, where Δ equals to 2.75 or 2 depending on the extent of degeneracy and is closely related to the carrier concentration[4]. For the Cu-free PbTe sample, its electron concentration is much less than 1×10^{19} cm^{-3} over the entire temperature range, and Δ equals to 2.75 representing low-degenerate behavior (see **Figure S4**d). However, for the Cu-intercalated PbTe samples with an electron concentration higher than 1×10^{19} cm^{-3} (the samples with x=0.005 and 0.006), Δ decreases to 2, which is consistent with the model for degenerate electrons scattered by acoustic phonons [see **Figure S4**b and c]. Therefore, for our Cu-doped PbTe system, the carrier concentration of 1×10^{19} cm^{-3} can be considered as a dividing line for the distinct temperature-dependent behaviors of carrier mobility. This is perfectly confirmed in the samples with 0.1 at% and 0.2 at% Cu, in which the magnitude of carrier concentration leaps from 1×10^{18} to 1×10^{19} with increasing temperature. The temperature-dependent carrier-mobility values of these two samples can be roughly divided into two regions (below 500 K and above 500 K, respectively) as shown in **Figure S4**b and c. In the temperature region of 300 K < T < 500 K, where the carrier concentrations are below 1×10^{19} cm^{-3}, Δ is ~ 2.75. However, when the carrier concentrations exceed 1×10^{19} cm^{-3} above 500 K, Δ changes to ~ 2, which is the same as that of the samples with 0.5 at% and 0.6 at% Cu. Therefore, it can be concluded that the interstitial Cu only increases the carrier concentration of the PbTe sample but has almost no influence on the carrier-scattering mechanism, which guarantees a relatively high

carrier mobility and thus superior electrical-transport properties in the Cu-intercalated PbTe sample.

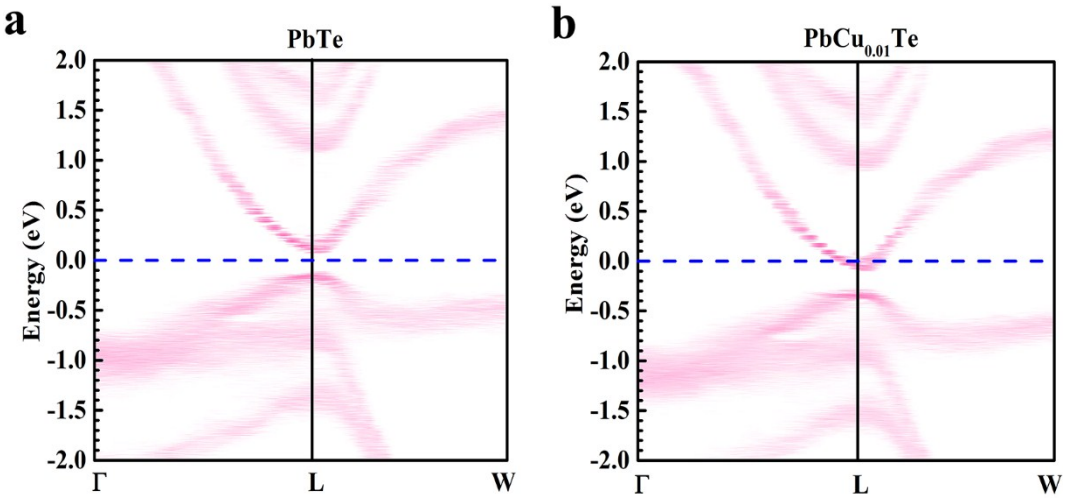

Figure S5. Electronic band structures at 800 K for (a) PbTe and (b) $PbCu_{0.01}Te$. All of the Fermi levels are set to be the zero energy points. Each band structure is obtained by averaging the band structures for 16 snapshots in the *ab initio* molecular dynamics. Calculation details can be found in our previous report[5].

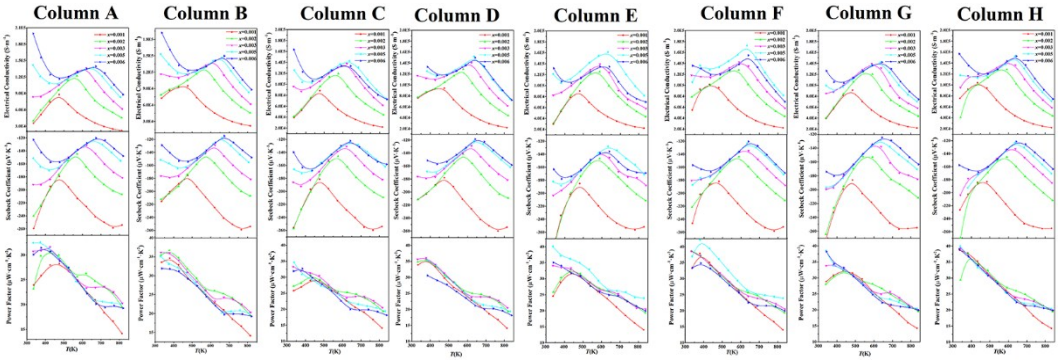

Figure S6. Repeatedly measured temperature dependence of electrical-transport properties of the $PbCu_xTe$ samples (x=0.001, 0.002, 0.003, 0.005, and 0.006). Columns A, C, E, and G are the measured data during the first to the fourth heating processes, respectively. Columns B, D, F, and H are the measured data during the first to the fourth cooling processes, respectively.

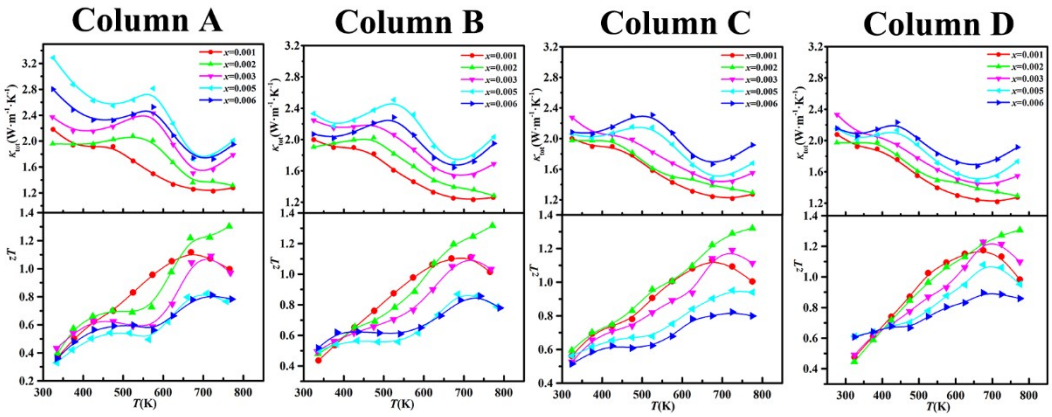

Figure S7. Repeatedly measured temperature dependence of total thermal conductivity and figure of merit zT of $PbCu_xTe$ (x=0.001, 0.002, 0.003, 0.005, and 0.006) samples. Columns A to D denote the first to the fourth heating processes, respectively.

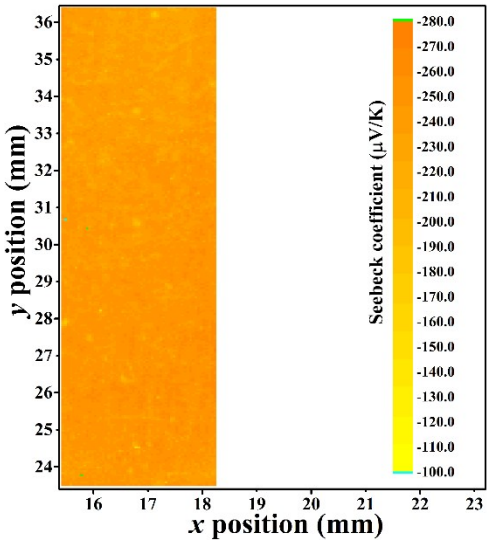

Figure S8. Seebeck coefficient mapping of the $PbTeCu_{0.002}$ sample after 4 cycling measurements.

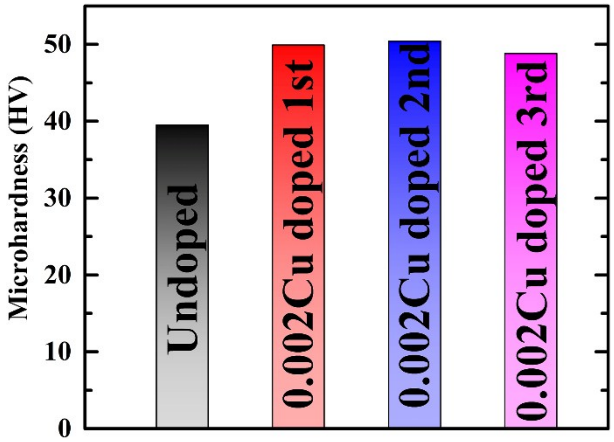

Figure S9. Room temperature Vickers hardness for Cu-free sample and 0.2 at% Cu doped PbTe sample. Note that the 0.2 at% Cu doped sample was repeatedly characterized after two thermal shocks in a vaccum quartz tube (heating up to 773 K at 10 K/min and kept at this temperature for 20 min with subsequent furnace cooling) .

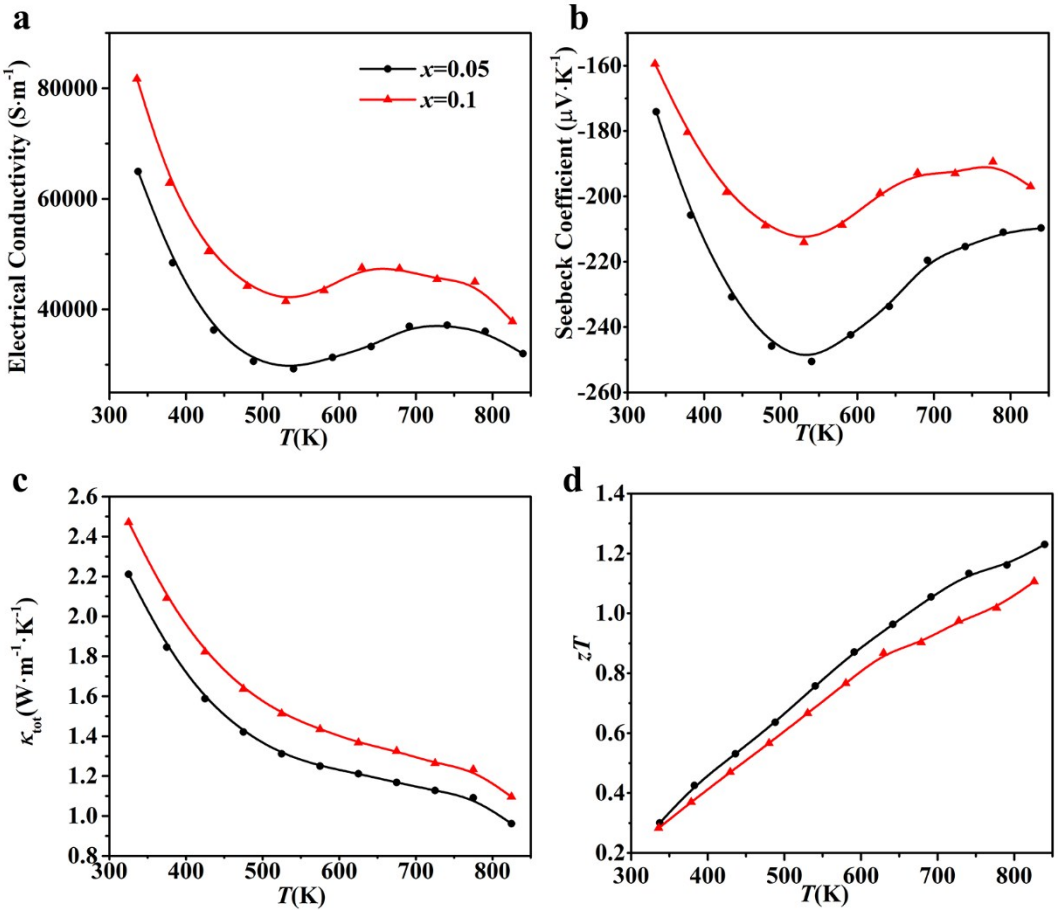

Figure S10. Thermoelectric properties of the 5 at% and 10 at% Cu-intercalated PbTe samples. Temperature-dependent (a) electrical conductivity, (b) Seebeck coefficient, (c) total thermal conductivity, and (d) figure of merit zT of the $PbCu_xTe$ (x=0.05 and 0.1) samples.

Supplementary Note 4: Calculation of the electrical-transport and thermoelectric-transport properties of n-type Cu-intercalated PbTe by the single Kane band model.

The thermoelectric-transport properties of n-type PbTe can be modeled by adopting the single Kane band model (SKB)[4],[6]. This model assumes that acoustic phonon scattering dominates the charge transport. For the SKB model, the thermoelectric-transport parameters are expressed as follows:

Seebeck coefficient: $S = \frac{k_B}{e}\left(\frac{{}^{1}F_{-2}^{1}}{{}^{0}F_{-2}^{1}} - \eta\right)$

Carrier concentration: $n = \frac{(2m^{*}k_BT)^{3/2}}{3\pi^{2}\hbar^{3}}\,{}^{0}F_{0}^{3/2}$

Carrier mobility: $\mu = \frac{2\pi \hbar^4 e C_l}{m_I^* (2 m_b^* k_B T)^{3/2} \Xi^2} \frac{3\,{}^0F_{-2}^1}{{}^0F_0^{3/2}}$

Hall factor A ($n = A \times n_{\mathrm{H}}$): $A = \frac{3K(K+2)}{(2K+1)^2} \frac{{}^0F_{-4}^{1/2}\,{}^0F_0^{3/2}}{({}^0F_{-2}^1)^2}$

Power factor: $PF = \frac{2N_V \hbar k_B^{\,2} C_l}{\pi \Xi^2 m_I^*} \left(\frac{{}^1F_{-2}^1}{{}^0F_{-2}^1} - \eta\right)^2 {}^0F_{-2}^1$

Figure of merit zT: $zT = \frac{\left(\frac{{}^1F_{-2}^1}{{}^0F_{-2}^1} - \eta\right)^2}{\left[\frac{{}^2F_{-2}^1}{{}^0F_{-2}^1} - \left(\frac{{}^1F_{-2}^1}{{}^0F_{-2}^1}\right)^2\right] + \frac{1}{3\,{}^0F_{-2}^1 B}}$

$$B = \frac{2T k_B^{\,2} \hbar C_l N_V}{3\pi m_I^{\,*} \Xi^2 \kappa_L}$$

In the above equations, the integral F is defined by:

$${}^nF_l^m = \int_0^\infty \left(-\frac{\partial f}{\partial \varepsilon}\right) \varepsilon^n (\varepsilon + \alpha\varepsilon^2)^m \left[(1+2\alpha\varepsilon)^2 + 2\right]^{l/2} d\varepsilon$$

where η is the reduced chemical potential defined by the equation $\eta = u/k_BT$, m^* is the density of state effective mass, inertial mass $m_I^* = 3(1/m_{//}^* + 2/m_{\perp}^*)$, band mass $m_b^* = N_V^{-2/3} m^* = (m_{//}^* m_{\perp}^{*})^{1/3}$, N_V is the band degeneracy, ε is the reduced energy of the electron state, and α ($\alpha = k_BT/E_g$) is the reciprocal reduced band separation responsible for the nonparabolicity of the band. E_g is the direct band gap at the L point of the Brillouin zone, which increases with the temperature according to the formula $E_g/eV = 0.17 + 4\times10^{-4} T/K$ for n-type PbTe. K is the band anisotropy factor defined by $K = m_{//}^*/m_{\perp}^*$, C_l is the longitudinal elastic moduli, and Ξ is the deformation potential. For the conduction band of PbTe, N_v=4, K=3.6, C_l=7.1×10[10] Pa, and Ξ=22 eV are used for modeling in this work[6]. The calculated results for the carrier concentration-dependent power factors and zT values are illustrated in **Figure S11**.

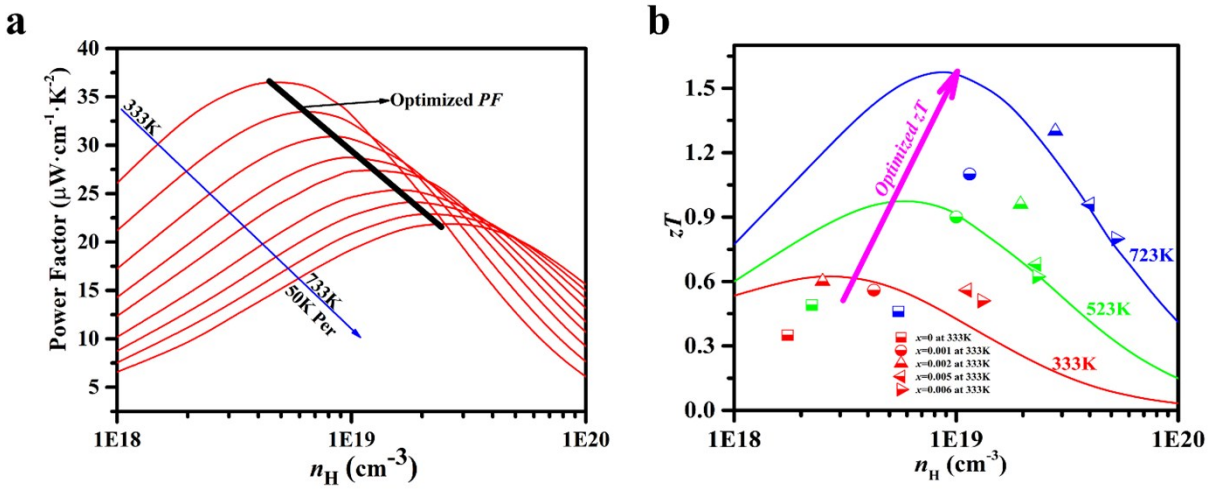

Figure S11. Calculated carrier concentration-dependent power factors and figure of merit *zT*. (a) Power-factor and (b) *zT* values of Cu-intercalated PbTe samples at different temperatures. The colored solid lines in (b) are predicted from the SKB model. The half-filled symbols of different colors in (b) are the experimental data at 333 K (red), 523 K (green), and 723 K (blue), respectively.

References

[1]C. C. Li, F. Drymiotis, L. L. Liao, H. T. Hung, J. H. Ke, C. K. Liu, C. R. Kao, G. J. Snyder, J. Mater. Chem. C 2015, 3, 10590.

[2]R. C. Weast, CRC handbook of chemistry and physics, CRC Press, Boca Raton, FL 1988.

[3]R. Dalven, Infrared Physics 1969, 9, 141.

[4]I. U. I. Ravich, B. A. Efimova, I. A. Smirnov, Semiconducting lead chalcogenides, Plenum Press, New York, 1970.

[5]L. You, Y. F. Liu, X. Li, P. F. Nan, B. H. Ge, Y. Jiang, P. F. Luo, S. S. Pan, Y. Z. Pei, W. Q. Zhang, G. J. Snyder, J. Yang, J. Y. Zhang, J. Luo, Energy Environ. Sci. 2018, 11, 1848.

[6]Y. Z. Pei, A. D. LaLonde, H. Wang, G. J. Snyder, Energy Environ. Sci. 2012, 5, 7963.